Sphere-Shaped Mn_3O_4 Catalyst with Remarkable Low-Temperature Activity for Methyl−Ethyl−Ketone Combustion

Hua Pan,[†,∥] Yanfei Jian,[†,∥] Changwei Chen,[†] Chi He,[*,†,‡] Zhengping Hao,[§] Zhenxing Shen,[†] and Hongxia Liu[†]

[†]Department of Environmental Science and Engineering, State Key Laboratory of Multiphase Flow in Power Engineering, Xi'an Jiaotong University, Xi'an, 710049, P.R. China

[‡]Cardiff Catalysis Institute, School of Chemistry, Cardiff University, Main Building, Park Place, Cardiff, CF10 3AT, U.K.

[§]Department of Environmental Nano-materials, Research Center for Eco-Environmental Sciences, Chinese Academy of Sciences, Beijing 100085, China

* Supporting Information

ABSTRACT: Mn_3O_4, $FeMnO_x$, and FeO_x catalysts synthesized via a solvothermal method were employed for catalytic oxidation of methyl−ethyl−ketone (MEK) at low temperature. Mn_3O_4 with sphere-like morphology exhibited the highest activity for MEK oxidation, over which MEK was completely oxidized to CO_2 at 200 °C, and this result can be comparable to typical noble metal loaded catalysts. The activation energy of MEK over Mn_3O_4 (30.8 kJ/mol) was much lower than that of $FeMnO_x$ (41.5 kJ/mol) and FeO_x (47.8 kJ/mol). The dominant planes, surface manganese species ratio, surface-absorbed oxygen, and redox capability played important roles in the catalytic activities of catalysts, while no significant correlation was found between specific surface area and MEK removal efficiency. Mn_3O_4 showed the highest activity, accounting for abundant oxygen vacancies, low content of surface Mn^{4+} and strong reducibility. The oxidation of MEK to CO_2 via an intermediate of diacetyl is a reaction pathway on Mn_3O_4 catalyst. Due to high efficiency and low cost, sphere-shaped Mn_3O_4 is a promising catalyst for VOCs abatement.

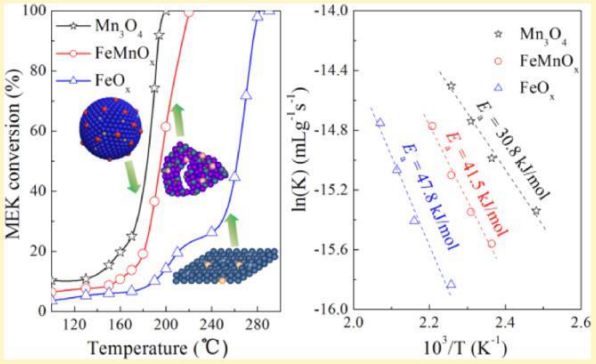

1. INTRODUCTION

Volatile organic compounds (VOCs) emitted from many industrial processes and transportation activities are considered a major source of photochemical smog, ozone depletion, and ground-level ozone generation.[1,2] Among the present tech-nologies for VOCs removal, catalytic combustion appears to be one of the most effective and energy-saving techniques due to its potential to completely convert pollutants into CO_2 and H_2O at low operating temperatures.[3−5]

Methyl−ethyl−ketone (MEK) is a ketone widely used as solvent in many industrial applications. However, it is hazardous and its emission to the atmosphere has to be controlled according to environmental regulations. In recent years, many studies have focused on the catalytic oxidation of MEK.[6−14] The noble-metal based catalysts, such as Pt/NaX,[6] Pt/Al-pillared clays,[7] PdO_x-MnO_x/Al_2O_3,[8] and Pd−Ce/ZSM-5,[9] have already exhibited activity for MEK oxidation in the previous studies. However, high cost and unstable at high temperatures prevent the noble metals from wide industrial applications. In contrast, transition metal oxides are considered as a promising candidate due to their low cost and excellent stability in practical applications. Some transition metal oxides catalysts (e.g., V_2O_5−P_2O_5,[10] La-transition metal (Cr, Co, Ni, Mn) perovskites,[11] Fe_2O_3,[12] Mn/γ-Al_2O_3,[13] and Cr/ZrO_2[14]) have already been investigated in the previous studies. Nevertheless, more toxic byproducts of MEK, for example, diacetyl (DAC), have been identified for catalytic oxidation of MEK on transition metal oxides.[8,9] Meanwhile, high operation temperature also limits the application of existing transition metal oxides catalyst. Thus, it is necessary and important to design novel transition metal oxides catalysts with excellent low-temperature activity and elucidate the catalytic reaction mechanisms to avoid and control the formation of reaction byproducts.

Within the transition metal oxide catalysts, manganese oxides present very interesting properties as catalyst for VOCs total oxidation because of the multiple different coordination numbers and oxidation states that Mn can adopt, as well as the presence of defects (primarily oxygen vacancies).[15] Gandhe et al.[16] showed that cryptomelane type manganese oxides, also called octahedral molecular sieve (OMS-2), had a highly

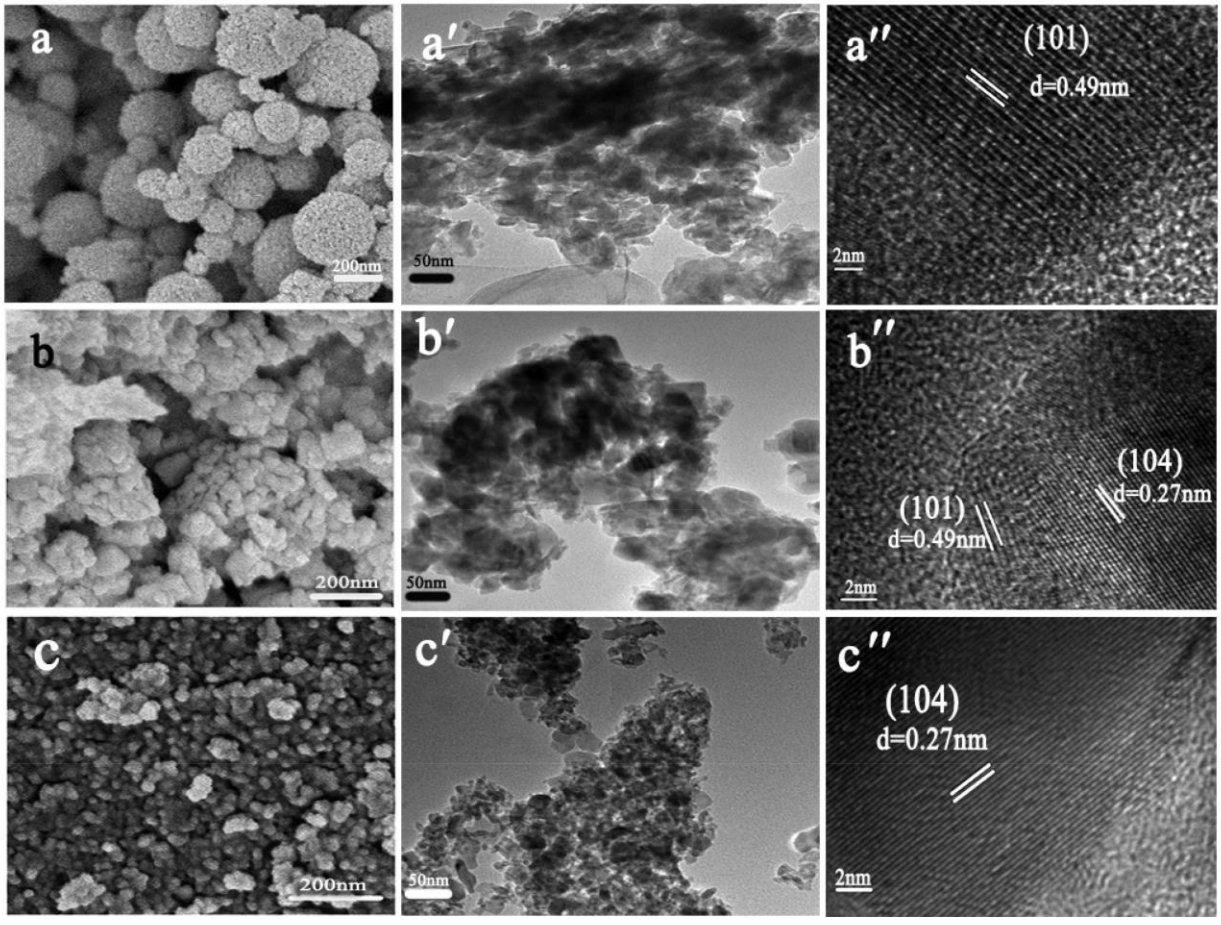

Figure 1. FE-SEM and HR-TEM images of (a, a', a") Mn_3O_4, (b, b', b") $FeMnO_x$, and (c, c', c") FeO_x samples.

efficient activity for the total oxidation of ethyl acetate, which was ascribed to the presence of Mn^{4+}/Mn^{3+} type redox couples and facile lattice oxygen on catalysts. A template-free oxalate route was applied to synthesize mesoporous manganese oxides with high surface area (355 $m^2\ g^{-1}$) and well-defined mesopores by Tang et al.[17] They found that the optimum mole ratio of Mn^{4+}/Mn^{2+} on mesoporous manganese oxides was close to 1.0 for VOC complete oxidation. Catalytic combustion of benzene and toluene was studied over manganese oxide catalysts (Mn_3O_4, Mn_2O_3 and MnO_2) by Kim and Shim.[18] The sequence of catalytic activity was as follows: $Mn_3O_4 > Mn_2O_3 > MnO_2$, which was correlated with the oxygen mobility on the catalyst. Piumetti et al.[19] reported three mesoporous manganese oxide catalysts (Mn_2O_3, Mn_3O_4 and Mn_xO_y) prepared by the solution combustion synthesis for the total oxidation of VOCs (ethylene, propylene, toluene and their mixture). The best catalytic activity was also achieved with the Mn_3O_4 catalyst, which showed the highest amount of electrophilic oxygen on the surface (O_α-species).

Additionally, iron-based catalysts, for example, , Fe/HfTi,[20] Fe/Ti-PILC,[21] mesoporous α-Fe_2O_3,[22] and iron-functionalized disordered mesoporous silica (FeKIL-2),[23] are known to exhibit good activity in the combustion of VOCs and also considered as environmentally friendly materials, because more than one valence states of the iron (Fe^{3+} and Fe^{2+}) could promoted the mutual transformation between the electrons and formation of oxygen vacancy caused by charge mismatching, resulting in formation of chemisorbed oxygen. To develop cost-effective approach, the transition metal (e.g., manganese and iron) oxides catalysts may be potential and promising for MEK combustion.

The textural property of metal oxides, including micro-morphology, exposed crystal plane, and crystallinity, is associated with their catalytic behavior. The morphology-controlling strategy has become a new approach for tuning the catalytic performance of oxides and oxide incorporating catalysts.[24,25] Recent research indicated that sphere-shaped metal oxides represent a new class of powerful catalysts, because of their high surface area, low density, easy recovery, self-supporting capacity, and surface permeability.[26−28] The preparation method is a critical factor to control the morphology of catalysts and dispersion of active sites.[29−31] A solvothermal synthesis technique was proposed for the preparation of sphere-shaped transition metal oxides used in other catalysis, such as sphere α-Fe_2O_3/MWCNT as photo-catalyst for the degradation of rhodamine B,[32] sphere MnO_x for room-temperature oxidation of HCHO,[33] and sphere-like $NiCo_2O_4$ for eolectro-catalytic oxidation of methanol.[34] This route paved the possible way for the formation of sphere-shaped manganese and/or iron oxides with high low-temperature catalytic activity and CO_2 selectivity in MEK combustion. Up to our knowledge, there is no literature reporting the catalytic combustion of MEK over sphere-like transition metal oxides.

In this work, we described a sphere-like Mn_3O_4 catalyst via a solvothermal reaction as an efficient catalyst for combustion of MEK. The relationship between physicochemical properties

and catalytic behavior and mechanisms of MEK combustion were investigated by various catalyst characterizations.

2. EXPERIMENTAL SECTION

The detailed experimental section is described in the Supporting Information (SI) (Text S1).

3. RESULTS AND DISCUSSION

3.1. Correlation of Physicochemical Property and Catalytic Activity.

3.1.1. Structural Properties. The morphologies of Mn_3O_4, $FeMnO_x$ and FeO_x samples were investigated by FE-SEM and HR-TEM, as shown in Figure 1. Mn_3O_4 possessed a submicrometer sphere-like morphology with the average diameter of around 400 nm (Figure 1a). The sphere-shaped Mn_3O_4 was resulting from the aggregation of fine grains of Mn_3O_4 with average diameter of around 40 nm (Figure 1a'). When iron was introduced, the morphology of $FeMnO_x$ turned into agglomeration structure consisting of a cluster of nanoparticles with the size of about 40 nm (Figure 1b and 1b'). However, the nanoparticles were observed with the small size in the range of 20−30 nm for FeO_x (Figure 1c and 1c'). In Figure 1a", the clear (101) lattice fringe with an interplanar spacing of 0.49 nm reveals that Mn_3O_4 is mainly enclosed by the (101) planes, which was also observed on manganese oxides (E-450: NaOH route) synthesized by Tang et al.[17] $FeMnO_x$ possesses a surface lattice spacing of 0.49 and 0.27 nm for the (101) and (104) crystal planes, respectively (Figure 1b"). Figure 1c" shows a clear (104) lattice fringe with an interplanar spacing of 0.27 nm on FeO_x, implying FeO_x is mainly enclosed by (104) facets.

Figure 2 shows the XRD patterns of the Mn_3O_4, $FeMnO_x$ and FeO_x catalysts. For $FeMnO_x$ sample, the peaks at 24.3°,

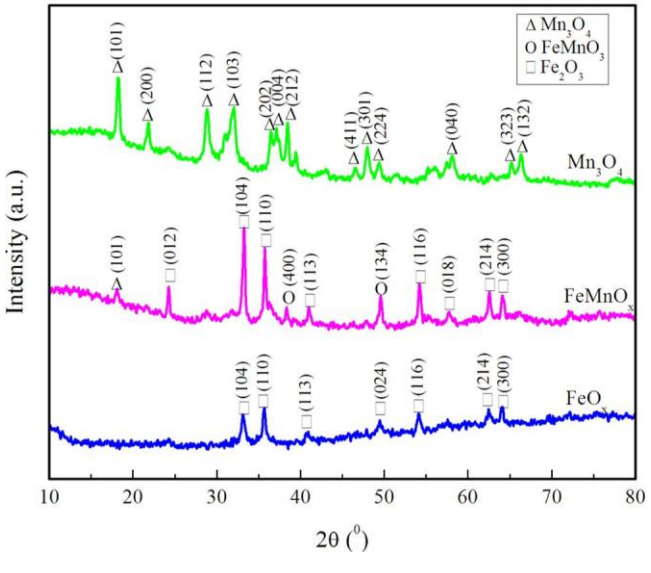

Figure 2. XRD patterns of Mn_3O_4, $FeMnO_x$, and FeO_x.

33.3°, 35.7°, 41.0°, 54.2°, 57.4°, 62.6°, and 64.2° correspond to the (012), (104), (110), (113), (116), (018), (214), (300) plane diffraction patterns of Fe_2O_3 (ICDD #01−079−0007), respectively. The diffraction peaks centered at 2θ of 38.3° and 49.5° over $MnFeO_3$ can be assigned to the (400) and (134) planes, respectively (ICDD #01-076-0076). Only one peak at 18.1° corresponds to the (101) plane diffraction pattern of Mn_3O_4 (ICDD #00-016-0350). This may be due to the fact that the Mn oxides were in a highly dispersed state. Compared with $FeMnO_x$, the diffraction intensities of Fe_2O_3 significantly decreased for FeO_x, indicating the smaller size of FeO_x nanocrystal. The full width at half-maximum of the peaks for $FeMnO_x$ was narrower than that of FeO_x, also meaning that the grain size of Fe_2O_3 on $FeMnO_x$ was larger than that on FeO_x, similar to the results of SEM (Figure 1). For Mn_3O_4, a strong diffraction peak of the (101) plane appeared significantly. It implies the thickness of crystal perpendicular to the (101) plane orientation over Mn_3O_4 is greater than that over $FeMnO_x$.

SI Figure S1 shows that all samples exhibit typical irreversible type IV shape isotherms. The condensation step on the isotherm at relative pressure of P/P_0 = 0.6−0.9 is the characteristic of capillary condensation of framework-confined mesopores, and the condensation step on the isotherm at P/P_0 higher than 0.9 indicates the presence of textural pores contributing to the filling of interparticle spaces.[35] Mn_3O_4 and $FeMnO_x$ displayed H3-type hysteresis cycles at P/P_0 = 0.8−1.0, indicating the coexistence of structural and interparticle accumulation mesopores (average pore size (D_p)) = 19.4 and 19.0 nm for Mn_3O_4 and $FeMnO_x$, respectively, SI Table S1). FeO_x exhibited H2 hysteresis loops at P/P_0 = 0.6−0.9, suggesting the presence of large amounts of structural mesopores (D_p = 9.2 nm, SI Table S1). The BET surface area and pore volume were listed in Table S1. FeO_x possessed the largest surface area (92.7 m^2/g) and smallest pore volume (0.22 cm^3/g), followed by $FeMnO_x$ (47.1 m^2/g, 0.25 cm^3/g) and Mn_3O_4 (46.9 m^2/g, 0.28 cm^3/g). It was consistent with the results of SEM (Figure 1), which the smallest size of nanoparticles were observed for FeO_x.

3.1.2. Surface Properties. XPS was conducted to characterize the chemical state of the elements in the near-surface region. Deconvolution of the Mn $2p_{3/2}$, Fe $2p_{3/2}$, and O 1s peak from each sample was performed by fitting a Gaussian−Lorentzian (GL) function with a Shirley background in Figure 3. The results from deconvolution (i.e., molar ratios of metal oxide species) are presented in Table 1.

Figure 3a illustrates XPS spectra of Mn 2p region for Mn_3O_4 and $FeMnO_x$ samples. For Mn_3O_4 catalyst, the binding energies of Mn $2p_{3/2}$ and Mn $2p_{1/2}$ were observed at 641.4 and 653.2 eV, respectively, which are characteristic XPS peaks of Mn_3O_4, and the splitting width (11.8 eV) is consistent well with the earlier report.[36] According to literature,[17,37,38] manganese species at binding energies (BE) = 640.6 ± 0.2, 641.7 ± 0.2, and 643 ± 0.2 eV were assigned to the surface Mn^{2+}, Mn^{3+}, and Mn^{4+} species, respectively. Thus, no surface Mn^{2+} species was detected on both Mn_3O_4 and $FeMnO_x$ catalysts. The oxide species of Mn^{4+} (642.8 eV) and Mn_3O_4 (641.4 eV) were obtained on the surface of Mn_3O_4 sample, whereas Mn^{4+} (642.8 eV) and Mn^{3+} (641.6 eV) species were found on the surface of $FeMnO_x$ sample. As shown in Table 1, the ratios of Mn^{4+}/ Mn_3O_4 and Mn^{4+}/Mn^{3+} on the surface of MnO_x and $FeMnO_x$ were approximately 0.75 and 1.00, respectively. It is remarkable to note that the intensities of Mn^{4+} characteristic peaks increased with the addition of Fe. The differences in the content of surface Mn^{4+} may result in the different perform-ances between MnO_x and $FeMnO_x$ sample on catalytic activity.

Fe $2p_{3/2}$ spectra for FeO_x and $FeMnO_x$ is presented in Figure 3b. Peaks located near 711.5 and 710 eV were assigned to Fe^{3+} and Fe^{2+},[39−41] respectively, indicating that iron species in FeO_x and $FeMnO_x$ are present both as Fe^{3+} and Fe^{2+}. The molar ratios of Fe^{2+}/Fe^{3+} on the surface of $FeMnO_x$ and FeO_x were approximately 2.00 and 0.80, respectively (Table 1). It

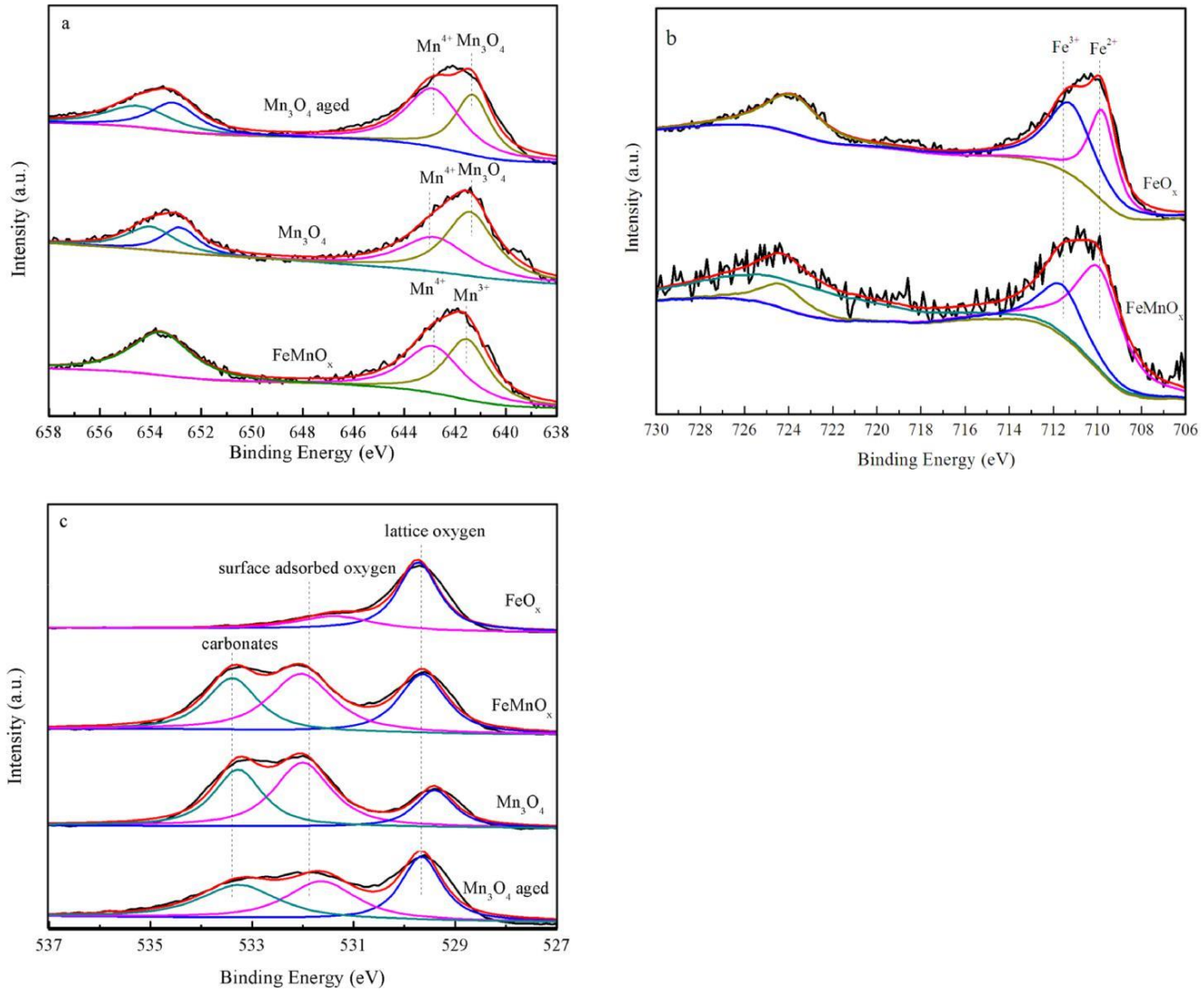

Figure 3. XPS spectra of (a) Mn 2p, (b) Fe 2p, and (c) O 1s regions for the samples.

Table 1. XPS Results of Catalysts

	binding energy (eV)							molar ratio			
sample	Mn_3O_4	Mn^{3+}	Mn^{4+}	Fe^{2+}	Fe^{3+}	O_{sur}	O_{latt}	Fe^{2+}/Fe^{3+}	Mn^{4+}/Mn^{3+}	Mn^{4+}/Mn_3O_4	O_{sur}/O_{latt}
Mn_3O_4	641.4		642.8			532.0	529.4			0.75	2.45
$FeMnO_X$		641.6	642.8	709.9	711.6	532.0	529.6	2.00	1.00		1.33
FeO_X				709.8	711.2	531.4	529.7	0.80			0.37
Mn_3O_4 aged	641.4		642.9			531.6	529.6			1.49	1.01

demonstrated that the intensity of Fe^{2+} characteristic peak increases with the addition of Mn.

As shown in Figure 3c, the fitted O 1s spectra displayed three major oxygen contributions with the corresponding peaks centered at 529.4−530.2 eV, 531.4−532.1 eV, and ~533.5 eV.[42,43] These bands can be attributed to lattice oxygen (O_{lat}), surface-absorbed oxygen stemmed from oxygen vacancies (O_{sur}),[42,43] and carbonates (O_{car}),[42,44] respectively. Compared with Mn_3O_4 and $FeMnO_X$, an obvious shift of the surface-absorbed oxygen peak toward lower binding energy was observed on FeO_X. It is worth noting that the lattice oxygen are nucleophilic reagents and are usually responsible for selective oxidation reactions. Conversely, electrophilic surface-absorbed oxygen (O_2^{2-}, O^-, and O_2^-), which implies the formation of radicals, are highly reactive and give rise to the total oxidations,[45−47] especially at temperatures below 400 °C.[48] Thus, surface-absorbed oxygen stemmed from the oxygen vacancies has higher mobility than lattice oxygen[18,49] and greatly influences the redox property of catalyst.[50] In Table 1, the ratio of O_{sur}/O_{lat} is approximately 0.37, 1.33, and 2.45 for FeO_X, $FeMnO_X$, and Mn_3O_4, respectively. It confirmed that a large amount of surface-adsorbed oxygen species existed on Mn_3O_4.

Samples of Mn_3O_4, $FeMnO_X$, and FeO_X were further characterized by Raman spectroscopy, which is powerful tool to probe vibrational behavior of lattices and hence probe structural differences in oxides, as displayed in Figure 4. The Raman band centered at 651 cm^{-1} over Mn_3O_4 and $FeMnO_X$

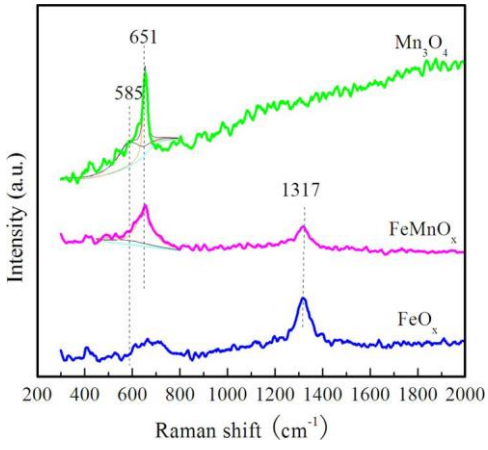

Figure 4. Raman spectra of Mn_3O_4, FeMnOx, and FeOx catalysts.

catalysts can be attributed to the Mn_2O_3 phase,[51] and the band at 1317 cm^{-1} over FeMnOx and FeOx samples can be assigned to the Fe_2O_3 phase in multi phonon mode.[52] The oxygen vacancy concentration in oxide catalysts has been indirectly measured in the literature in the region of 585 cm^{-1}.[53,54] The relevant peaks of the synthesized catalysts were deconvoluted using a Gaussian method, and the corresponding peak areas are shown in SI Table S1. It can be seen that the oxygen vacancy concentration follows the order Mn_3O_4 > FeMnOx ≫ FeOx, which correlates well with the O 1s result (Table 1). The formation of oxygen vacancies has a significant influence on MEK oxidation. These defective sites can act as active centers in MEK oxidation reaction as the adsorbed oxygen molecules over oxygen vacancies tend to be readily transferred and subsequently replenish the consumed O^{2-} species in the bulk catalysts timely.

3.1.3. Reducibility. H_2-TPR was employed to investigate the redox ability of Mn_3O_4, FeMnOx, and FeOx catalysts, as shown in Figure 5. The reduction behavior of these catalysts was very

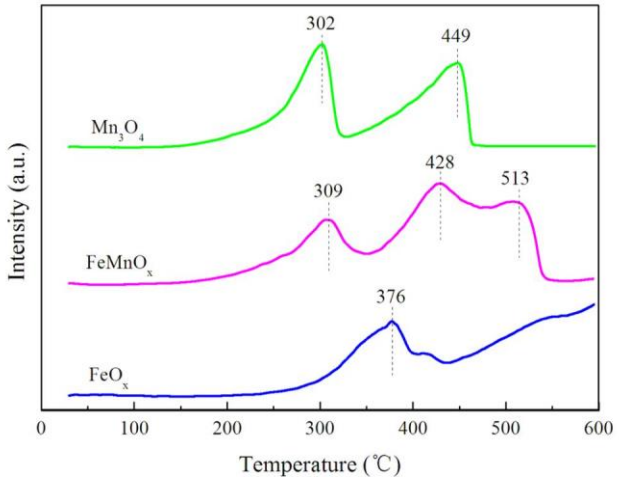

Figure 5. H_2-TPR profile of Mn_3O_4, FeMnOx, and FeOx catalysts.

different. For Mn_3O_4, two peaks centered at 302 and 449 °C was ascribed to the reduction of MnO_2 to Mn_3O_4[42,55,56] and Mn_3O_4 to MnO,[56,57] respectively. FeOx showed one peak at 376 °C, which may correspond to the reduction of Fe^{3+} to Fe^{2+}.[39,58] Compared with Mn_3O_4, the reduction peak of MnO_2 (309 °C) shifted to higher temperatures for FeMnOx. The peaks at 428 and 513 °C were attributed to the reduction of Mn_3O_4 and Fe^{2+}, respectively. According to the area and temperature of reduction peaks, the reducibility of catalysts decreased in the order of Mn_3O_4 > FeMnOx > FeOx.

3.1.4. Catalytic Performance. The evaluation of the catalytic activities on the oxidation of MEK is shown in Figure 6(a). The MEK oxidation activity increased with an increase in reaction temperature. T_{50} and T_{90} (the reaction temperature corre-sponding to MEK conversion of 50% and 90%, respectively) were used to compare the catalytic activities of the samples. For Mn_3O_4, FeMnOx, and FeOx samples, the values of T_{50} are 182, 196, and 262 °C, respectively, and T_{90} are 194, 215, and 276 °C, respectively. The apparent activation energy (Ea) was also introduced to compare the low-temperature activity of our samples, because the catalyst with lower Ea value could cause MEK to be oxidized more readily. The Ea values were calculated under the low MEK conversion (<25%) at temperature range of 130 170 °C, 150 180 °C, and 170 210 °C for Mn_3O_4, FeMnOx, and FeOx samples, respectively. As shown in Figure 6(b). The Ea value increased in the order of Mn_3O_4 (30.8 kJ/mol) < FeMnOx (41.5 kJ/mol) < FeOx (47.8 kJ/mol). In SI Table S2, MEK conversion rates of our samples decreased in the order of Mn_3O_4 (3.97×10^{-4} mmol mL_{cat}^{-1} h^{-1}) > FeMnOx (1.96×10^{-4} mmol mL_{cat}^{-1} h^{-1}) > FeOx (4.88×10^{-4} mmol mL_{cat}^{-1} h^{-1}). Therefore, it can be deduced that the activities of the three samples decreased in the order of Mn_3O_4 > FeMnOx > FeOx. If compared to other catalysts reported in the literature (SI Table S2), the outstanding activity of sphere-like Mn_3O_4 prepared in this work was apparent. For example, Mn/γ-Al_2O_3 had T_{50} of 195 °C and T_{90} of 375 °C for MEK combustion.[13] Catalysts of α-Fe_2O_3 (T_{50} of 230 °C, T_{90} of 250 °C and Ea of 117 kJ mol^{-1})[12] and Cr/ZrO_2 (T_{50} of 230 °C and Ea of 55.2 kJ mol^{-1})[14] were also less active than sphere-shaped Mn_3O_4 catalyst reported in the present paper. Therefore, although this comparison has to be taken with caution because of the different reaction conditions employed, our sphere-shaped Mn_3O_4 catalyst exhibited the highest catalytic activity among the non-noble metal loaded catalysts reported for this catalytic system. Even compared with the noble metal loaded catalysts, both MEK conversion and CO_2 yield rate of our sphere-shaped Mn_3O_4 were higher than noble metal loaded catalysts reported.[6−9] T_{50} (182 and 189 °C based on MEK conversion and CO_2 yield, respectively), T_{90} (194 and 198 °C based on MEK conversion and CO_2 yield, respectively) and Ea (30.8 kJ mol^{-1}) of our sphere-shaped Mn_3O_4 were lower than those (T_{50} = 190 °C and T_{90} = 205 °C based on CO_2 yield) over Pt/NaX,[6] (T_{50} = 210 °C and T_{90} = 265 °C based on MEK conversion) over Pt/BAsap,[7] (T_{50} = 292 °C, T_{90} = 305 °C and Ea = 117 kJ mol^{-1} based on CO_2 yield) over Pd−Mn/Al_2O_3,[8] and (T_{50} = 210 °C and T_{90} = 226 °C based on MEK conversion) over Pd−Ce/ZSM-5,[9] but a little higher than those (T_{50} = 170 °C and T_{90} = 190 °C based on CO_2 yield) over Pt/OMS-2.[15]

In Figure 6(c), CO_2 yield increased with an increase in reaction temperature on the three samples, which was similar to MEK conversion. Interestingly, MEK was completely oxidized to CO_2 over Mn_3O_4 catalyst at 200 °C, and no partial oxidation products were detected, as substantiated by the good carbon balance (ca. 99.5%). Additionally, CO_2 yields of 98.8% and 92.1% were obtained on FeMnOx at 220 °C and FeOx at 290 °C, respectively. If taking T_{50}' and T_{90}' as the temperature at which CO_2 yield is 50% and 90%, respectively, the activities of the three samples also decreased as follows: Mn_3O_4 (T_{50}': 189

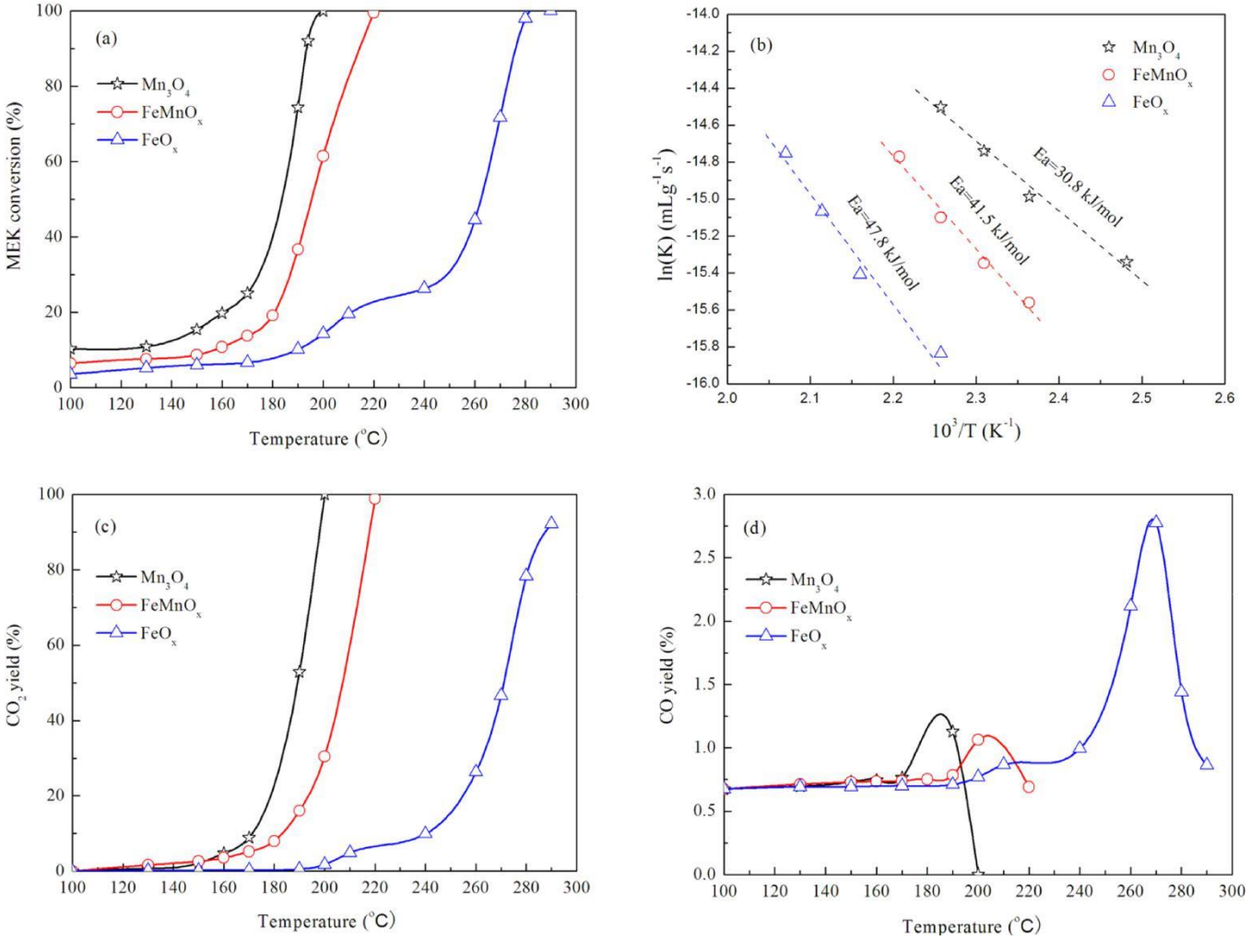

Figure 6. Ignition curves (a), Ea (b), CO_2 (c), and CO (d) yield for MEK oxidation over Mn_3O_4, $FeMnO_x$, and FeO_x catalysts.

°C; T_{90}': 198 °C) > $FeMnO_x$ (T_{50}': 207 °C; T_{90}': 218 °C)> FeO_x (T_{50}': 271 °C; T_{90}': 287 °C). It further demonstrates that Mn_3O_4 catalyst is a promising catalyst for the low-temperature catalytic oxidation of MEK. Figure 6(d) presents CO yield from MEK combustion over all samples. Unlike the curves of MEK conversion and CO_2 yield, CO yield showed a "volcano-shaped" curve, and low conversion of MEK to CO was observed over all samples. Maximum CO yields of only 1.13%, 1.06%, and 2.77% were detected on Mn_3O_4, $FeMnO_x$ and FeO_x catalysts, respectively. It means that CO yield does not always increase with reaction temperature rising. No or only a little CO was formed at the optimum operation temperature (e.g., T_{90} and T_{100}). It is of importance in the catalytic combustion of VOCs.

The excellent catalytic results for MEK oxidation obtained with sphere-shaped Mn_3O_4 catalyst can be due to several factors that are intimately correlated. Considering that the catalytic activities of samples, the growth of plentiful (101) planes (Figures 1 and 2) are the active facets for MEK combustion on Mn_3O_4 catalyst. Concerning the influence of surface area, Mn_3O_4 with the smallest surface area (SI Table S1) exhibited the highest activity among the samples. It implies that surface area is not the important factor influencing the catalytic performance of our samples, although surface area is widely considered as a critical factor for catalysts applica-tions.[5,20−22] As previously stated, sphere-shaped Mn_3O_4 catalyst presented the highest concentration of surface-absorbed oxygen (Figure 3c and Table 1) and oxygen defects (Figure 4 and SI Table S1) among our samples. Compared fresh Mn_3O_4, the ratio of O_{sur}/O_{lat} decreased significantly for Mn_3O_4 used after the stability test (Figure 3c and Table 1), suggesting that a large amount of surface-adsorbed oxygen species take part in the catalytic reaction of MEK combustion. The surface-absorbed oxygen originated from the oxygen vacancies has higher mobility than lattice oxygen[18,49] and greatly influences the redox property of catalyst.[50] Thus, sphere-shaped Mn_3O_4 displayed greatest catalytic activity, due to more surface-absorbed oxygen stemmed from oxygen vacancies. Compare with $FeMnO_x$, the lower content of Mn^{4+} was detected on the surface of Mn_3O_4 (see Figure 3a and Table 1). Piumetti et al.[19] also found the lowest Mn^{4+}/Mn^{3+} ratio on Mn_3O_4, which exhibited the highest activity for the total oxidation of VOCs among three mesoporous manganese oxide catalysts (Mn_2O_3, Mn_3O_4 and Mn_xO_y). Therefore, the lower loading of surface Mn^{4+} also resulted in the high activity of sphere-shaped Mn_3O_4. Finally, the excellent low-temperature reducibility of Mn_3O_4 sample (Figure 5) improved the catalytic performance for MEK oxidation at low temperature. The combination of above properties in sphere-shaped Mn_3O_4 catalyst (the plentiful (101) planes, low content of surface Mn^{4+}, abundant oxygen vacancies, and strong reducibility) could explain its excellent behavior as low temperature MEK combustion catalyst.

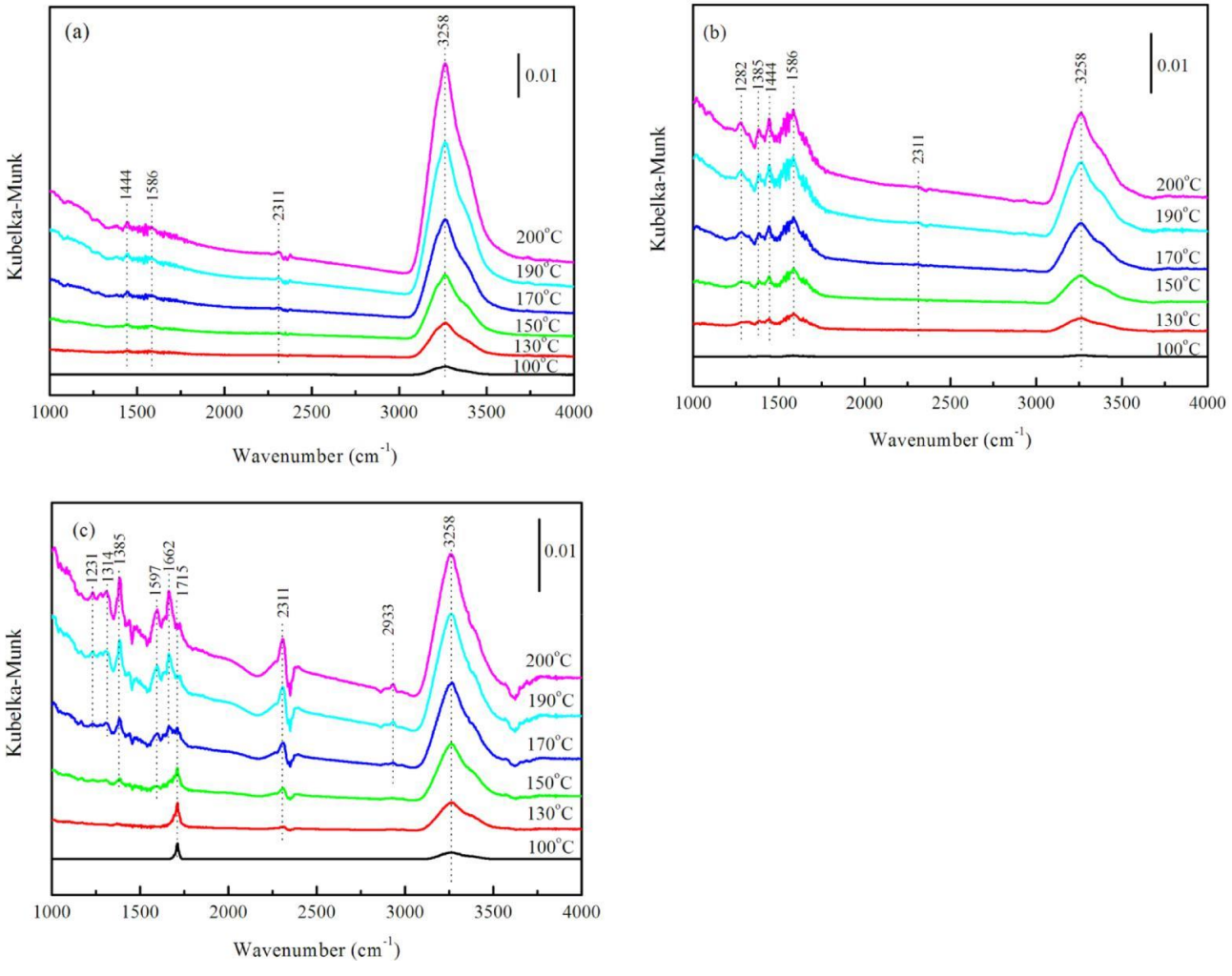

Figure 7. DRIFT spectra of MEK combustion on (a) Mn_3O_4, (b) $FeMnO_x$ and (c) FeO_x.

Catalyst stability is an important criterion for industrial applications. SI Figure S2a shows the stability test of Mn_3O_4 catalyst at T_{90} (194 °C) and GHSV of 25,440 h^{-1} for 30 h. Mn_3O_4 displayed the excellent stability for MEK combustion, and only a slight decrease of MEK conversion from 93% to 89% was observed in the first few hours. The good stability provides the possibility for the practical elimination of MEK. Coke deposition on Mn_3O_4 after stability test was determined by TGA (SI Figure S2b). The weight loss (0.4 wt %) in temperature range of 50−150 °C of the fresh sample can be attributed to the desorption of H_2O and oxygen. The aged sample displayed two stages of weight losses with the first stage from 170 to 210 °C and second one from 550 to 600 °C. The first stage of weight loss (0.7 wt %) might be attributed to combustion/desorption of MEK adsorbed on the aged sample, as well as the desorption of O_2 and H_2O. The second stage small weight loss (0.3 wt %) was correspond to the combustion of coke deposited on catalyst. Slight decrease in BET surface area and pore volume were observed for the aged sample (SI Table S1).

3.2. Mechanisms. In order to evaluate the oxidation behavior of MEK more accurately, TPSR of MEK oxidation was carried out and the results were illustrated in SI Figure S3. TPSR profiles of diacetyl (m/z = 43) and CO_2 (m/z = 44) were detected on both Mn_3O_4 and $FeMnO_x$. The intensity of diacetyl initially increased with temperature rising up to 150 °C, and then decreased greatly with further increasing of temperature. The intensity of CO_2 increased significantly with the whole temperature region. It indicated that diacetyl is a main intermediate for MEK oxidation on both Mn_3O_4 and $FeMnO_x$. Compared with Mn_3O_4 and $FeMnO_x$, the lower intensity of TPSR profile was detected on FeO_x, because MS profile was measured at temperature from 100 to 210 °C. MEK conversion was significantly low on FeO_x at temperature range between 100 and 210 °C (Figure 6). New MS profiles of m/z = 41 and 74 was observed on FeO_x, which could be assigned to $CH_3COC(CH_3)CH_2$ and CH_3COOCH_3, respectively. Interest-ingly, $CH_3COC(CH_3)CH_2$ (m/z = 41) presented a similar changing trend with CO_2 (m/z = 44) over FeO_x. It seems that $CH_3COC(CH_3)CH_2$ is a main intermediate in MEK oxidation on FeO_x.

The mechanisms of MEK oxidation over synthesized catalysts were further investigated by in situ FT-IR spectros-copy, as displayed in Figure 7. For Mn_3O_4 catalyst (Figure 7a), a strong peak of 3258 cm^{-1} was due to OH stretching of the Brønsted acid.[59,60] Brønsted acid sites are very important in oxidation catalysis, since the surface acidity, as well as the basic properties, may be responsible for the adsorption/desorption rates of reactants and products, and are a major factor in the activation of hydrocarbons and occurring intermediates.[61] The lowest intensity of OH stretching of the Brønsted acid (3258 cm^{-1}) was detected for MEK oxidation on Mn_3O_4 catalyst at

Scheme 1. Mechanisms of MEK Combustion on Samples

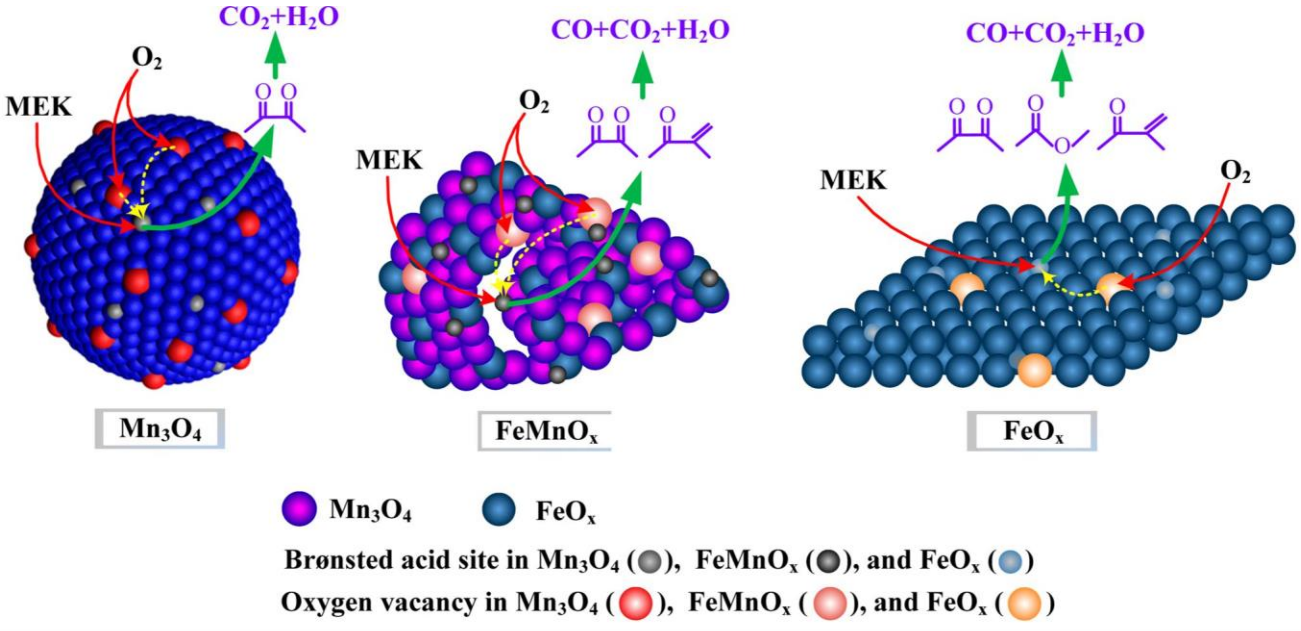

100 °C. It suggests that MEK is initially adsorbed on the Brønsted acid sites of Mn_3O_4, resulting in the obvious intensity loss of the acidic hydroxyl groups (3258 cm^{-1}) at low temperature of 100 °C. The peak intensity of 3258 cm^{-1} (OH stretching of the Brønsted acid) significantly increased with reaction temperature increasing from 100 to 200 °C, because of the oxidation of MEK adsorbed on the Brønsted acid sites. Weak bands at 2311, 1586, and 1444 cm^{-1} were assigned to CO_2,[62] C O stretching vibrations of β-diketone ligands,[63,64] and surface carbonate species,[19] respectively. According to the results of TPSR (SI Figure S3), the band of 1586 cm^{-1} (C O stretching vibrations of β-diketone ligands) stemmed from diacetyl ($CH_3COCOCH_3$), which was a common reaction intermediate in catalytic oxidation of MEK.[8] It indicates that the oxidation of MEK to CO_2 via an intermediate of trace diacetyl is a reaction pathway on Mn_3O_4 catalyst (Scheme 1).

In Figure 7b, IR bands at 3258, 2311, 1586, and 1444 cm^{-1} cm^{-1} were also observed on FeMnOx catalyst, which was similar to Mn_3O_4. Additionally, two new bands at 1385 and 1282 cm^{-1} corresponding to ν_s(COO) stretching[65] and $\delta_s(CH_2)$,[66] respectively, appeared in the oxidation of MEK on FeMnOx. From MS signal (SI Figure S3), the band of $\delta_s(CH_2)$ originated from $CH_3COC(CH_3)CH_2$, which was also an intermediate.[9] The intensity of all bands increased significantly when temperature was raised, except for the band of CO_2 (2311 cm^{-1}). It suggests MEK oxidation to CO_2 on FeMnOx includes two reaction pathways in parallel via intermediates of diacetyl and $CH_3COC(CH_3)CH_2$, as shown in Scheme 1.

As shown in Figure 7c, the same trend of bands at 3258 cm^{-1} was observed on FeO_x. The relatively strong intensity of band at 2311 cm^{-1} (CO) was detected, implying inhibition of CO desorption on FeO_x catalyst. C O stretching vibrations of -diketone ligands (1597 cm^{-1}) and ν_s(COO) stretching (1385 cm^{-1}) was also found on FeO_x,[63,64] indicating the formation of diacetyl. Compared with DRIFT of Mn_3O_4 and $FeMnO_x$, more bands appeared on FeO . The bands at 2933, 1715, and 1662 were attributed to the vibrations of CH ((CH)), C O vibrations (ν(C O)),[68] the bending vibration of OH^- species from the water,[69] respectively. IR bands at 1314 and 1231 cm^{-1} also corresponded to ν (COO) stretching.[70] Based on the results of TPSR (SI Figure S3), ν(C O) (1715) and ν_s(COO) (1314 and 1231 cm^{-1}) stemmed from $CH_3COC(CH_3)CH_2$ and CH_3COOCH_3, respectively. It implied that MEK oxidation process was complex on FeO_x, including three reaction pathways in parallel via intermediates of diacetyl, $CH_3COC(CH_3)CH_2$ and CH_3COOCH_3 (Scheme 1).

ASSOCIATED CONTENT

* Supporting Information

Experimental Section; Textural properties and Raman results; Reaction rate, T_{50}, T_{90}, and Ea for MEK oxidation; N_2 adsorption/desorption isotherms of catalysts; Stability and TGA profiles of the fresh and aged samples; TPSR of MEK oxidation (PDF)

AUTHOR INFORMATION

Corresponding Author

* Phone/fax: 86 29 82663857; e-mail: chi_he@xjtu.edu.cn.

ORCID

Chi He: 0000-0001-6403-1277

Author Contributions

‖These authors contributed equally to this work.

Notes

The authors declare no competing financial interest.

ACKNOWLEDGMENTS

This work was financially supported by the National Natural Science Foundation of China (21677114, 21477095, and 21337003), the National Key Research and Development Program (2016YFC0204201), the Natural Science Basic Research Plan in Shaanxi Province of China (2014JQ2-2009), and the Fundamental Research Funds for the Central Universities (xjj2017170, 2015gjhz10, and xjj2015132).

REFERENCES

(1) Park, J.-H.; Goldstein, A. H.; Timkovsky, J.; Fares, S.; Weber, R.; Karlik, J.; Holzinger, R. Active atmosphere-ecosystem exchange of the vast majority of detected volatile organic compounds. Science 2013, 341 (6146), 643−647.

(2) Yoon, J.; Chae, S. K.; Kim, J.-M. Colorimetric Sensors for volatile organic compounds (VOCs) based on conjugated polymer-embedded electrospun fibers. J. Am. Chem. Soc. 2007, 129 (11), 3038−3039.

(3) Rotter, H.; Landau, M. V.; Herskowitz, M. Combustion of chlorinated VOC on nanostructured chromia aerogel as catalyst and catalyst support. Environ. Sci. Technol. 2005, 39 (17), 6845−6850.

(4) Wang, R.; Li, J. Effects of precursor and sulfation on OMS-2 catalyst for oxidation of ethanol and acetaldehyde at low temperatures. Environ. Sci. Technol. 2010, 44 (11), 4282−4287.

(5) Si, W. Z.; Wang, Yu.; Zhao, S.; Hu, F. Y.; Li, J. H. A facile method for in situ preparation of the MnO_2/$LaMnO_3$ catalyst for the removal of toluene. Environ. Sci. Technol. 2016, 50 (8), 4572−4578.

(6) Guillemot, M.; Mijoin, J.; Mignard, S.; Magnoux, P. Volatile organic compounds (VOCs) removal over dual functional adsorbent/ catalyst system. Appl. Catal., B 2007, 75 (3−4), 249−255.

(7) Gil, A.; Vicente, M. A.; Lambert, J.-F.; Gandía, L. M. Platinum catalysts supported on Al-pillared clays-Application to the catalytic combustion of acetone and methyl-ethyl-ketone. Catal. Today 2001, 68 (1−3), 41−51.

(8) Arzamendi, G.; de la Pena O Shea, V. A.; Alvarez-Galvan, M. C.; Fierro, J. L. G.; Arias, P. L.; Gandía, L. M. Kinetics and selectivity of methyl-ethyl-ketone combustion in air over alumina-supported PdO_x-MnO_x catalysts. J. Catal. 2009, 261 (1), 50−59.

(9) Yue, L.; He, C.; Zhang, X. Y.; Li, P.; Wang, Z.; Wang, H. L.; Hao, Z. P. Catalytic behavior and reaction routes of MEK oxidation over Pd/ZSM-5 and Pd-Ce/ZSM-5 catalysts. J. Hazard. Mater. 2013, 244− 245, 613−620.

(10) Ai, M. Oxidation of methyl ethyl ketone to diacetyl on V_2O_5-P_2O_5 catalysts. J. Catal. 1984, 89 (2), 413−421.

(11) Alvarez-Galvan, M. C.; de la Pena O Shea, V. A.; Arzamendi, G.; Pawelec, B.; Gandía, L. M.; Fierro, J. L. G. Methyl ethyl ketone combustion over La-transition metal (Cr, Co, Ni, Mn) perovskites. Appl. Catal., B 2009, 92 (3−4), 445−453.

(12) Escobar, G. P.; Beroy, A. Q.; Iritia, M. P. P.; Huerta, J. H. Kinetic study of the combustion of methyl-ethyl ketone over alpha-hematite catalyst. Chem. Eng. J. 2004, 102 (2), 107−117.

(13) Salari, D.; Niaei, A.; Hosseini, S. A.; Aleshzadeh, R.; Afshary, H. Remediation of various naturally oxygenated volatile organic compounds (O-VOCS) by Mn- and Cr-supported γ-Al_2O_3 nano-catalysts. Turk. J. Chem. 2011, 35 (5), 793−802.

(14) Choudhary, V. R.; Deshmukh, G. M. Kinetics of the complete combustion of dilute propane and methyl ethyl ketone over Cr-doped ZrO_2 catalyst. Chem. Eng. Sci. 2005, 60 (6), 1575−1581.

(15) Sanz, O.; Delgado, J. J.; Navarro, P.; Arzamendi, G.; Gandía, L. M.; Montes, M. VOCs combustion catalysed by platinum supported on manganese octahedral molecular sieves. Appl. Catal., B 2011, 110, 231−237.

(16) Gandhe, A. R.; Rebello, J. S.; Figueiredo, J. L.; Fernandes, J. B. Manganese oxide OMS-2 as an effective catalyst for total oxidation of ethyl acetate. Appl. Catal., B 2007, 72 (1−2), 129−135.

(17) Tang, W. X.; Wu, X. F.; Li, D. Y.; Wang, Z.; Liu, G.; Liu, H. D.; Chen, Y. F. Oxalate route for promoting activity of manganese oxide catalysts in total VOCs' oxidation: effect of calcination temperature and preparation method. J. Mater. Chem. A 2014, 2 (8), 2544−2554. (18) Kim, S. C.; Shim, W. G. Catalytic combustion of VOCs over a series of manganese oxide catalysts. Appl. Catal., B 2010, 98 (3−4), 180−185.

(19) Piumetti, M.; Fino, D.; Russo, N. Mesoporous manganese oxides prepared by solution combustion synthesis as catalysts for the total oxidation of VOCs. Appl. Catal., B 2015, 163 (2015), 277−287. (20) Tsoncheva, T.; Ivanova, R.; Henych, J.; Velinov, N.; Kormunda, M.; Dimitrov, M.; Paneva, D.; Slusna, M.; Mitov, I.; Stengl, V. Iron modified titanium-hafnium binary oxides as catalysts in total oxidation of ethyl acetate. Catal. Commun. 201620165, 81, 14−19.10.1016/ j.catcom.2016.03.014

(21) Liang, X. L.; Qi, F. H.; Liu, P.; Wei, G. L.; Su, X. L.; Ma, L. Y.; He, H. P.; Lin, X. J.; Xi, Y. F.; Zhu, J. X.; Zhu, R. L. Performance of Ti-pillared montmorillonite supported Fe catalysts for toluene oxidation: The effect of Fe on catalytic activity. Appl. Clay Sci. 2016, 132−133, 96−104.

(22) Solsona, B.; García, T.; Sanchis, R.; Soriano, M. D.; Moreno, M.; Rodríguez-Castellon, E.; Agouram, S.; Dejoz, A.; Lopez Nieto, J. M. Total oxidation of VOCs on mesoporous iron oxide catalysts: Soft chemistry route versus hard template method. Chem. Eng. J. 2016, 290, 273−281.

(23) Rangus, M.; Mazaj, M.; Drazic, G.; Popova, M.; Tusar, N. N. Active iron sites of disordered mesoporous silica catalyst FeKIL-2 in the oxidation of volatile organic compounds (VOC). Materials 2014, 7 (6), 4243−4257.

(24) Zhou, K. B.; Li, Y. D. Catalysis based on nanocrystals with well-defined facets. Angew. Chem., Int. Ed. 2012, 51 (3), 602−613.

(25) Xie, X. W.; Li, Y.; Liu, Z. Q.; Haruta, M.; Shen, W. J. Low-temperature oxidation of CO catalysed by Co_3O_4 nanorods. Nature 2009, 458 (7239), 746−749.

(26) Chen, X. Y.; Yang, W. L.; Wang, S.; Qiao, M. H.; Yan, S. R.; Fan, K. N.; He, H. Y. Amorphous Ni-B hollow spheres synthesized by controlled organization of Ni-B nanoparticles over PS beads via surface seeding/electroless plating. New J. Chem. 2005, 29 (2), 266−268.

(27) Bai, Z. Y.; Yang, L.; Li, L.; Lv, J.; Wang, K.; Zhang, J. A facile preparation of hollow palladium nanosphere catalysts for direct formic acid fuel cell. J. Phys. Chem. C 2009, 113 (24), 10568−10573.

(28) Song, C. Y.; Zhao, G. P.; Zhang, P. J.; Rosi, N. L. Expeditious synthesis and assembly of sub-100 nm hollow spherical gold nanoparticle superstructures. J. Am. Chem. Soc. 2010, 132 (40), 14033−14035.

(29) Li, J. H.; Hao, J. M.; Fu, L. X.; Liu, Z. M.; Cui, X. Y. The activity and characterization of sol-gel Sn/Al_2O_3 catalyst for selective catalytic reduction of NO_X in the presence of oxygen. Catal. Today 2004, 90 (3−4), 215−221.

(30) Shi, L. M.; Chu, W.; Qu, F. F.; Luo, S. H. Low-temperature catalytic combustion of methane over MnO_x-CeO_2 mixed oxide catalysts: Effect of preparation method. Catal. Lett. 2007, 113 (1−2), 59−64.

(31) Tang, X. F.; Li, Y. G.; Huang, X. M.; Xu, Y. D.; Zhu, H. Q.; Wang, J. G.; Shen, W. J. MnO_x-CeO_2 mixed oxide catalysts for complete oxidation of formaldehyde: Effect of preparation method and calcination temperature. Appl. Catal., B 2006, 62 (3−4), 265−273.

(32) Zhao, Z.; Zhou, X. W.; Liu, Z., Synthesis of Nanosphere alpha-Fe_2O_3/MWCNT composite as Photo-catalyst for the Degradation of Rhodamine B. In Proceedings Of the 4th International Conference on Mechatronics, Materials, Chemistry And Computer Engineering 2015, Liang, Z.; Li, X., Eds., 2015; Vol. 39, pp 2317−2321.10.2991/ icmmcce-15.2015.444

(33) Wang, J. L.; Zhang, P. Y.; Li, J. G.; Jiang, C. J.; Yunus, R.; Kim, J. Room-Temperature Oxidation of Formaldehyde by Layered Man-ganese Oxide: Effect of Water. Environ. Sci. Technol. 2015, 49 (20), 12372−12379.

(34) Gu, L.; Qian, L.; Lei, Y.; Wang, Y. Y.; Li, J.; Yuan, H. Y.; Xiao, D. Microwave-assisted synthesis of nanosphere-like $NiCo_2O_4$ consisting of porous nanosheets and its application in electro-catalytic oxidation of methanol. J. Power Sources 2014, 261, 317−323.

(35) He, C.; Xu, B. T.; Shi, J. W.; Qiao, N. L.; Hao, Z. P.; Zhao, J. L. Catalytic destruction of chlorobenzene over mesoporous ACeOx (A = Co, Cu, Fe, Mn, or Zr) composites prepared by inorganic metal precursor spontaneous precipitation. Fuel Process. Technol. 2015, 130, 179−187.

(36) Yuan, Z. L.; Chen, S. H.; Liu, B. Nitrogen-doped reduced graphene oxide-supported Mn_3O_4: An efficient heterogeneous catalyst for the oxidation of vanillyl alcohol to vanillin. J. Mater. Sci. 2017, 52 (1), 164−172.

(37) Chen, Z. H.; Yang, Q.; Li, H.; Li, X. H.; Wang, L. F.; Tsang, S. C. Cr-MnO_x mixed-oxide catalysts for selective catalytic reduction of NO_x with NH_3 at low temperature. J. Catal. 2010, 276 (1), 56−65.

(38) Zhang, D. S.; Zhang, L.; Shi, L. Y.; Fang, C.; Li, H. R.; Gao, R. H.; Huang, L.; Zhang, J. P. In situ supported MnO_x-CeO_x on carbon nanotubes for the low-temperature selective catalytic reduction of NO with NH_3. Nanoscale 2013, 5 (3), 1127−1136.

(39) Pan, H.; Guo, Y.; Bi, H. T. NO_x adsorption and reduction with C_3H_6 over Fe/zeolite catalysts: effect of catalyst support. Chem. Eng. J. 2015, 280, 66−73.

(40) Shishkin, A.; Carlsson, P.-A.; Harelind, H.; Skoglundh, M. Effect of preparation procedure on the catalytic properties of Fe-ZSM-5 as SCR catalyst. Top. Catal. 2013, 56 (9−10), 567−575.

(41) Carrillo, A. I.; Serrano, E.; Luque, R.; Garcia-Martinez, J. Microwave-assisted catalysis by iron oxide nanoparticles on MCM-41: effect of the support morphology. Appl. Catal., A 2013, 453, 383−390.

(42) Jampaiah, D.; Ippolito, S. J.; Sabri, Y. M.; Reddy, B. M.; Bhargava, S. K. Highly efficient nanosized Mn and Fe codoped ceria-based solid solutions for elemental mercury removal at low flue gas temperatures. Catal. Sci. Technol. 2015, 5 (5), 2913−2924.

(43) Venkataswamy, P.; Rao, K. N.; Jampaiah, D.; Reddy, B. M. Nanostructured manganese doped ceria solid solutions for CO oxidation at lower temperatures. Appl. Catal., B 2015, 162, 122−132.

(44) Yao, X. J.; Yu, Q.; Ji, Z. Y.; Lv, Y. Y.; Cao, Y.; Tang, C. J.; Gao, F.; Dong, L.; Chen, Y. A comparative study of different doped metal cations on the reduction, adsorption and activity of CuO/$Ce_{0.67}M_{0.33}O_2$ (M = Zr^{4+}, Sn^{4+}, Ti^{4+}) catalysts for NO plus CO reaction. Appl. Catal., B 2013, 130, 293−304.

(45) Harris, K. D. M.; Edwards, P. P.; Turning Points in Solid-State Materials and Surface Science; RCS Publishing: Cambridge, 2008, 568− 576.

(46) Zawadzki, M.; Trawczynski, J. Synthesis, characterization and catalytic performance of LSCF perovskite for VOC combustion. Catal. Today 2011, 176 (1), 449−452.

(47) Liu, Y. X.; Dai, H. X.; Deng, J. G.; Xie, S. H.; Yang, H. G.; Tan, W.; Han, W.; Jiang, Y.; Guo, G. S. Mesoporous Co_3O_4-supported gold nanocatalysts: Highly active for the oxidation of carbon monoxide, benzene, toluene, and o-xylene. J. Catal. 2014, 309, 408−418.

(48) Fei, Z. Y.; Sun, B.; Zhao, L.; Ji, W. J.; Au, C. T. Strong morphological effect of Mn_3O_4 nanocrystallites on the catalytic activity of Mn_3O_4 and Au/Mn_3O_4 in benzene combustion. Chem. - Eur. J. 2013, 19 (20), 6480−6487.

(49) Chen, H.; Sayari, A.; Adnot, A.; Larachi, F. Composition-activity effects of Mn-Ce-O composites on phenol catalytic wet oxidation. Appl. Catal., B 2001, 32 (3), 195−204.

(50) Tan, H.; Wang, J.; Yu, S.; Zhou, K. Support morphology-dependent catalytic activity of Pd/CeO_2 for formaldehyde oxidation. Environ. Sci. Technol. 2015, 49 (14), 8675−8682.

(51) Ramana, S.; Rao, B. G.; Venkataswamy, P.; Rangaswamy, A.; Reddy, B. M. Nanostructured Mn-doped ceria solid solutions for efficient oxidation of vanillyl alcohol. J. Mol. Catal. A: Chem. 2016, 415, 113−121.

(52) Hadzic, B.; Romcevic, N.; Romcevic, M.; Kuryliszyn-Kudelska, I.; Dobrowolski, W.; Narkiewicz, U.; Sibera, D. Influence of SOP modes on Raman spectra of ZnO(Fe) nanoparticles. Opt. Mater. 2015, 42, 118−123.

(53) Marban, G.; Fuertes, A. B. Highly active and selective CuO_x/CeO_2 catalyst prepared by a single-step citrate method for preferential oxidation of carbon monoxide. Appl. Catal., B 2005, 57 (1), 43−53.

(54) He, C.; Yu, Y. K.; Chen, C. W.; Yue, L.; Qiao, N. L.; Shen, Q.; Chen, J. S.; Hao, Z. P. Facile preparation of 3D ordered mesoporous CuO_x-CeO_2 with notably enhanced efficiency for the low temperature oxidation of heteroatom-containing volatile organic compounds. RSC Adv. 2013, 3 (42), 19639−19656.

(55) Chlala, D.; Giraudon, J. M.; Nuns, N.; Lancelot, C.; Vannier, R. N.; Labaki, M.; Lamonier, J. F. Active Mn species well dispersed on Ca^{2+} enriched apatite for total oxidation of toluene. Appl. Catal., B 2016, 184, 87−95.

(56) Jiang, B.; Deng, B.; Zhang, Z.; Wu, Z.; Tang, X.; Yao, S.; Lu, H. Effect of Zr addition on the low-temperature SCR activity and SO_2 tolerance of Fe−Mn/Ti catalysts. J. Phys. Chem. C 2014, 118 (27), 14866−14875.

(57) Zhang, Z. F.; Liu, B. S.; Wang, F.; Wang, W. S.; Xia, C.; Zheng, S.; Amin, R. Hydrogen sulfide removal from hot coal gas by various mesoporous silica supported Mn_2O_3 sorbents. Appl. Surf. Sci. 2014, 313, 961−969.

(58) Sreekanth, P. M.; Smirniotis, P. G. Selective reduction of NO with CO over titania supported transition metal oxide catalysts. Catal. Lett. 2008, 122 (1−2), 37−42.

(59) Zhao, Y.; Zhao, B.; Zhuo, Y.; Chen, C.; Xu, X. A study of the mechanism of iron-based sulfate catalyst for selective catalytic reduction of NO with NH_3. Asia-Pac. J. Chem. Eng. 2012, 7 (4), 581−589.

(60) Long, R. Q.; Yang, R. T. Characterization of Fe-ZSM-5 catalyst for selective catalytic reduction of nitric oxide by ammonia. J. Catal. 2000, 194 (1), 80−90.

(61) Vedrine, J. C. The role of redox, acid base and collective properties and of cristalline state of heterogeneous catalysts in the selective oxidation of hydrocarbons. Top. Catal. 2002, 21 (1−3), 97− 106.

(62) Berna, A.; Kuzume, A.; Herrero, E.; Feliu, J. M. Ethylene adsorption and oxidation on Pt(h k l) in acidic media. Surf. Sci. 2008, 602 (1), 84−94.

(63) Pi, Y.; Wang, D. J.; Liu, H.; Hu, Y. J.; Wei, X. H.; Zheng, J. Synthesis and spectroscopic properties of some new difluoroboron bis-beta-diketonate derivatives. Spectrochim. Acta, Part A 2014, 131, 209− 213.

(64) Reutov, V. A.; Gukhman, E. V.; Kafitulova, E. E. Boron difluoride beta-diketonates: III. Boron difluoride 3-organylpenta-2,4-dionates. Russ. J. Gen. Chem. 2003, 73 (9), 1441−1444.

(65) Zou, X. L.; Rui, Z. B.; Song, S. Q.; Ji, H. B. Enhanced methane combustion performance over $NiAl_2O_4$-interfacepromoted Pd/γ-Al_2O_3. J. Catal. 2016, 338, 192−201.

(66) Dai, Q. G.; Yin, L. L.; Bai, S. X.; Wang, W.; Wang, X. Y.; Gong, X. Q.; Lu, G. Z. Catalytic total oxidation of 1,2-dichloroethane over VO_x/CeO_2 catalysts: Further insights via isotopic tracer techniques. Appl. Catal., B 2016, 182, 598−610.

(67) Zhang, R. D.; Shi, D. J.; Liu, N.; Cao, Y.; Chen, B. H. Mesoporous SBA-15 promoted by 3d-transition and noble metals for catalytic combustion of acetonitrile. Appl. Catal., B 2014, 146, 79−93.

(68) Kukulska-Zajac, E.; Gora-Marek, K.; Datka, J. IR and TPD studies of the reaction of acetic acid in zeolites NaHY. Microporous Mesoporous Mater. 2006, 96 (1−3), 216−221.

(69) Chen, H.; Tang, M.; Rui, Z.; Ji, H. MnO_2 Promoted TiO_2 nanotube array supported Pt catalyst for formaldehyde oxidation with enhanced efficiency. Ind. Eng. Chem. Res. 2015, 54 (36), 8900−8907.

(70) Ma, C. Y.; Pang, G. L.; He, G. Z.; Li, Y.; He, C.; Hao, Z. P. Layered sphere-shaped TiO_2 capped with gold nanoparticles on structural defects and their catalysis of formaldehyde oxidation. J. Environ. Sci. 2016, 39, 77−85.